

Large spin-relaxation anisotropy in bilayer-graphene/WS₂ heterostructures

S. Omar,^{1,*} B.N. Madhushankar,¹ and B.J. van Wees¹

¹The Zernike Institute for Advanced Materials University of Groningen Nijenborgh 4 9747 AG, Groningen, The Netherlands
(Dated: March 3, 2022)

We study spin-transport in bilayer-graphene (BLG), spin-orbit coupled to a tungsten di sulfide (WS₂) substrate, and measure a record spin lifetime anisotropy ~ 40 -70, i.e. ratio between the out-of-plane τ_{\perp} and in-plane spin relaxation time τ_{\parallel} . We control the injection and detection of in-plane and out-of-plane spins via the shape-anisotropy of the ferromagnetic electrodes. We estimate $\tau_{\perp} \sim 1$ -2 ns via Hanle measurements at high perpendicular magnetic fields and via a new tool we develop: Oblique Spin Valve measurements. Using Hanle spin-precession experiments we find a low $\tau_{\parallel} \sim 30$ ps in the electron-doped regime which only weakly depends on the carrier density in the BLG and conductivity of the underlying WS₂, indicating proximity-induced spin-orbit coupling (SOC) in the BLG. Such high τ_{\perp} and spin lifetime anisotropy are clear signatures of strong spin-valley coupling for out-of-plane spins in BLG/WS₂ systems in the presence of SOC, and unlock the potential of BLG/transition metal dichalcogenide heterostructures for developing future spintronic applications.

Keywords: Spintronics, Graphene, graphene-semiconductor interface, spin-orbit coupling, TMD

Graphene (Gr) in contact with a transition metal dichalcogenide (TMD), having high intrinsic spin-orbit coupling (SOC) offers a unique platform where the charge transport properties in Gr are well preserved due to the weak van der Waals interaction between the two materials. However, the spin transport properties are greatly affected due to the TMD-proximity induced SOC in graphene [1, 2, 8]. At the Gr/TMD interface, the spatial inversion symmetry is broken, and the graphene sublattices having K(K') valleys experience different crystal potentials and spin-orbit coupling magnitudes from the underlying TMD. The electron-spin degree of freedom and its interaction with other properties such as valley pseudospins in the presence of SOC provide access to spintronic phenomena such as spin-valley coupling [4–7, 9], spin-Hall effect [10, 11], (inverse) Rashba-Edelstein effect [12–16] and even topologically protected spin-states [17–21] which are not possible to realize in pristine graphene. The mentioned effects are sought after for realizing enhancement and electric field control of SOC [1, 4, 8, 22–25], efficient charge-current to spin-current conversion and vice versa [10, 27–29], which will be the building blocks for developing novel spintronic applications [13, 30].

Experiments on Gr/TMD systems confirm the presence of enhanced spin-orbit coupling [8, 31] and the anisotropy in the in-plane (τ_{\parallel}) and out-of-plane (τ_{\perp}) spin relaxation times [9, 32] in single layer graphene. Recent theoretical studies [22, 23] predict that due to the special band-structure of bilayer-graphene on a TMD substrate, it is expected to show a larger spin-relaxation anisotropy $\eta = \frac{\tau_{\perp}}{\tau_{\parallel}}$ even up to 10000 [23], which is approximately 1000 times higher than the highest reported η values for single-layer graphene-TMD heterostructures [9, 33]. As explained in Ref. [23], a finite band-gap opens up in bilayer-graphene (BLG) in presence of a built-in electric field at the BLG/TMD interface, which can be tuned via

an external electric field. The BLG valence (conduction) band is formed via the carbon atom orbitals at the bottom (top) layer. As a consequence, due to the closer proximity of the bottom BLG layer with the TMD, the BLG valence band has almost two order higher magnitude of SOC of spin-valley coupling character than the SOC in the conduction band. This modulation in the SOC can be accessed in two ways: either by the application of a back-gate voltage by tuning the Fermi energy or via the electric-field by changing the sign of the orbital-gap. Depending on whether the graphene is hole or electron doped, and the magnitude of the electric field at the interface, BLG can therefore exhibit the effect of spin-valley coupling in the magnitude of spin-relaxation anisotropy ratio η .

In this letter, we report the transport of both in-plane and out-of-plane spins in BLG supported on a TMD substrate, i.e. tungsten disulfide (WS₂). We inject and detect the out-of-plane spins in graphene via a purely electrical method by exploiting the magnetic shape anisotropy of the ferromagnetic electrodes at high magnetic fields [34–36], in contrast with the optical injection of out-of-plane spins into Gr/TMD systems in refs. [37, 38]. We extract $\tau_{\perp} \sim 1$ ns-2 ns, which results in $\eta = \frac{\tau_{\perp}}{\tau_{\parallel}} \sim 40$ -70 via two independent methods; Hanle measurements at high perpendicular magnetic field and a newly developed tool *Oblique Spin Valve* measurements. Such large η confirms the existence of strong spin-valley coupling for the out-of-plane spins in BLG/TMD systems. We find a weak modulation in both τ_{\parallel} and τ_{\perp} as a function of charge carrier density in the electron-doped regime in the BLG. τ_{\parallel} varies from 15-30 ps, with such short values indicating the presence of a very strong spin-orbit coupling in the BLG, induced by the WS₂ substrate.

Bilayer-graphene/WS₂ samples are prepared on a SiO₂/Si substrate (thickness $t_{\text{SiO}_2} \sim 500$ nm) via a dry

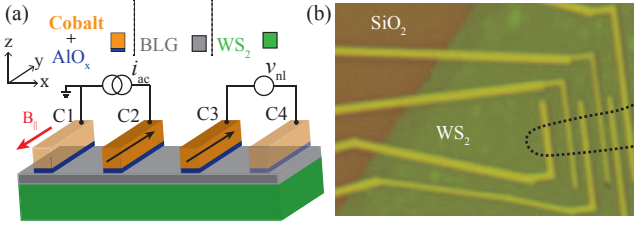


FIG. 1. (a) Nonlocal spin-transport measurement scheme. The ferromagnetic electrodes C2-C3 are premagnetized along the y-axis by applying an in-plane magnetic field. The outer electrodes C1 and C4 act as reference electrodes. (b) An optical image of a part of WS₂/BLG sample (stack A) where the measurements are performed. The BLG is outlined with a black dashed line which extends further to the right.

pick-up transfer method [2] (see Supplemental Material for fabrication details). We study two bottom-WS₂/BLG samples (thickness $t_{\text{WS}_2} \sim 3$ nm), labeled as stack A and stack B, and present the data from the left region of stack A (Fig. 1(b)) as a representative sample. Additional measurements from stack B and the right-side region of stack A are presented in Supplemental Material, also show similar results. We use a low-frequency ac lock-in detection method to measure the charge and spin transport properties of the graphene flake. In order to measure the I-V behavior of the bottom WS₂ flake and for gate-voltage application, a Keithley 2410 dc voltage source was used. All measurements are performed at Helium temperature (4 K) under vacuum conditions in a cryostat.

Details of charge and spin-transport measurement methods and TMD characterization are provided in Supplemental Material. We obtain the BLG electron-mobility $\mu_e \sim 3,000 \text{ cm}^2\text{V}^{-1}\text{s}^{-1}$, which is somewhat low compared to the previously reported mobility values in graphene on a TMD substrate [1, 8].

We perform spin-transport measurements, using the measurement scheme shown in Fig. 1(a) and measure the nonlocal signal $R_{\text{nl}} = v_{\text{nl}}/i_{\text{ac}}$. For in-plane spin transport, the spin-signal is defined as $R_{\text{nl}}^{\parallel} = \frac{R_{\text{nl}}^{\text{P}} - R_{\text{nl}}^{\text{AP}}}{2}$, where $R_{\text{nl}}^{\text{AP(P)}}$ is the R_{nl} measured for the (anti-)parallel magnetization orientations of the injector-detector electrodes. From non-local spin-valve (SV) and Hanle spin-precession measurements, we obtain the spin diffusion coefficient D_s and in-plane spin-relaxation time τ_{\parallel} , and estimate the spin-relaxation length $\lambda_s^{\parallel} = \sqrt{D_s \tau_{\parallel}}$. A representative Hanle measurement for stack A is shown in Fig. 2(b). Due to small magnitudes of in-plane spin-signals and invasive ferromagnetic (FM) contacts ($\sim 1\text{k}\Omega$), we were able to get information about the in-plane spins via Hanle measurements only for short injector-detector separation of about 1-2 μm . Since we could not access the hole-doped regime for the applied back-gate voltage due to heavily n-doped samples, we only measure

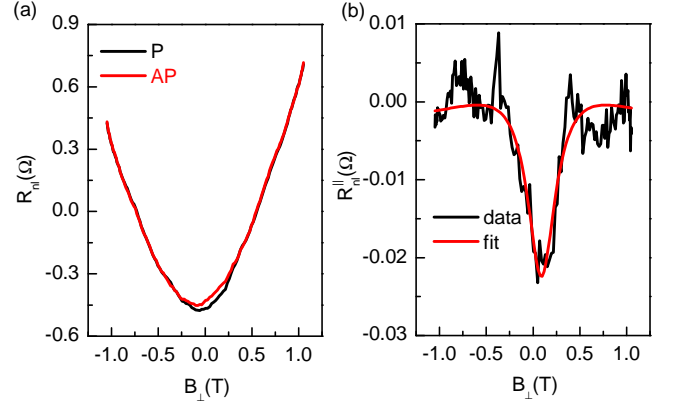


FIG. 2. (a) Parallel (P) and anti-parallel (AP) Hanle curves for $L = 1\mu\text{m}$ ($V_{\text{bg}} = 0\text{V}$) show a strong increase in the non-local resistance with the applied out-of-plane magnetic field B_{\perp} , which indicates a large spin-relaxation anisotropy and the high spin-relaxation time for the out-of-plane spins. Signs of P and AP configurations are reversed because one electrode has a negative contact-polarization for in-plane spins. (b) The Hanle spin-signal $R_{\text{nl}}^{\parallel}$ and the fit result in low $\tau_{\parallel} \sim 30\text{ps}$ (stack A).

the spin-transport in the electron-doped regime for both stacks. For stack A, we obtain $D_s \geq 0.01 \text{ m}^2\text{s}^{-1}$ and τ_{\parallel} in the range 18-34 ps, i.e. $\lambda_s^{\parallel} \sim 0.45\text{-}0.54 \mu\text{m}$. For stack B, we obtain $D_s \sim 0.03 \text{ m}^2\text{s}^{-1}$ and τ_{\parallel} in the range 17-24 ps, i.e. $\lambda_s^{\parallel} \sim 0.6\text{-}0.7 \mu\text{m}$. In conclusion, though for both samples we obtain reasonable charge transport properties, i.e. $D_s \sim 0.01 \text{ m}^2\text{s}^{-1}$, we obtain a very low τ_{\parallel} down to 16 ps. The weak modulation of τ_{\parallel} with the back-gate voltage suggests a strong SOC induced in the BLG in contact with WS₂ [1] and the insignificant contribution of the spin-absorption mechanism for the applied back-gate voltage range in contrast with the behavior observed in refs. [32, 40, 41].

In order to explore the proposed spin-relaxation anisotropy in BLG/WS₂ systems [23], we inject out-of-plane spins electrically by controlling the magnetization direction of the FM electrodes via an external magnetic field. Due to its finite shape anisotropy along the z-axis, the magnetization of the FM electrode does not stay in the device plane at high enough B_{\perp} . For the FM electrodes with the thickness ~ 65 nm, their magnetization can be aligned fully in the out-of-plane direction at $B_{\perp} \sim 1.5$ T [5, 34]. At $B_{\perp} \geq 0.3$ T, the magnetization makes an angle $\theta > 10^\circ$ with the easy-axis of the FM electrode, which increases with the field (see Supplemental Material for details). In this case, the injected spins, along with the dephasing in-plane spin-signal component as shown in Fig. 2(b) also have a non-precessing out-of-plane spin-signal component, which would increase with B_{\perp} due to the contact magnetization aligning towards B_{\perp} (Fig. 2(a)). From this measurement, we can estimate

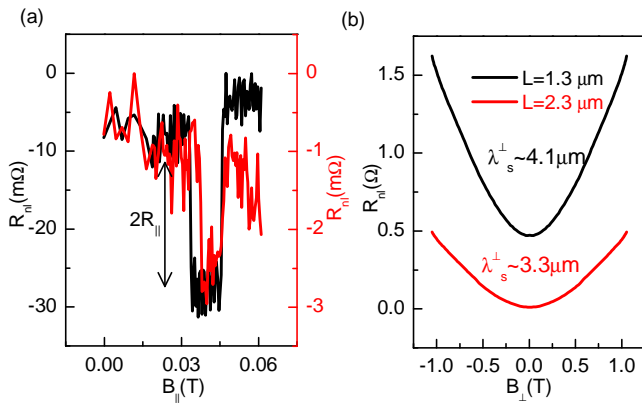


FIG. 3. (a) In-plane SV signals at the injector-detector separation $L = 1.3 \mu\text{m}$ (black) and $2.3 \mu\text{m}$ (red) with their values on the left and right axis, respectively. A background signal of 0.5Ω ($7\text{m}\Omega$) has been subtracted from the measured spin-signal at $L = 1.3(2.3) \mu\text{m}$ for a clear representation. (b) Measured and symmetrized Hanle curves for different L for the parallel configuration of FM electrodes.

τ_{\perp} by removing the contribution of the in-plane spin-signal and the background charge (magneto)resistance, i.e. $R_{\text{sq}}(B_{\perp})$ (for details, refer to Supplemental Material) and fit R_{nl} with the following equation:

$$R_{\text{nl}}(B_{\perp}) = \frac{P^2 R_{\text{sq}} \lambda_s^{\perp} e^{-\frac{L}{\lambda_s^{\perp}}} (\sin \theta)^2}{2w}. \quad (1)$$

Here $R_{\text{nl}}(B_{\perp})$ is the measured signal for out-of-plane spins for the injector-detector separation L , channel width w , with out-of-plane spin relaxation length λ_s^{\perp} . R_{sq} is the graphene sheet resistance at $B_{\perp} = 0$ T. We assume that both electrodes have equal spin-injection and detection polarization P , which we obtain in the range 3-5% via regular in-plane spin-transport measurements (see Supplemental Material for details).

BLG on TMD is expected to have $\tau_{\perp} \gg \tau_{\parallel}$ [23], which also implies that $R_{\text{nl}}(B_{\perp})$ at $\theta = \pi/2$, i.e. R_{nl}^{\perp} will be higher in magnitude than $R_{\text{nl}}^{\parallel}$ at $B_{\perp} = 0$. In our measurements, this effect reflects as a strong increase in R_{nl} at high B_{\perp} for both P and AP configurations (Fig. 2(a)). Via charge magnetoresistance measurements (see Supplemental Material) for the same channel, we confirm that the observed enhancement in R_{nl} is not due to the magnetoresistance originating from the orbital effects under the applied out-of-plane magnetic field. Next, we show the distance dependence of R_{nl} in Fig. 3. The in-plane spin signal $R_{\text{nl}}^{\parallel}$ is reduced almost by factor of ten from $10 \text{ m}\Omega$ to $1 \text{ m}\Omega$ (Fig. 3(a)). On the other hand, $R_{\text{nl}}(B_{\perp})$ for the same distance decreases roughly by less than factor of three. From this measurement, we confirm that $\tau_{\perp} \gg \tau_{\parallel}$ in the BLG/WS₂ heterostructures. We fit the experimental data in Fig. 3(b) with Eq. 1 for different L , and obtain $\lambda_s^{\perp} \sim 3.3 \mu\text{m} - 4.1 \mu\text{m}$. We extract τ_{\perp} from

the relation $\lambda_s^{\perp} = \sqrt{D_s \tau_{\perp}}$, while we assume equal D_s for in-plane and out-of-plane spins [32], and obtain $\tau_{\perp} \sim 1 \text{ ns} - 1.6 \text{ ns}$, resulting in a large anisotropy $\eta \sim 50-70$.

In order to confirm the spin life-time anisotropy in BLG/WS₂ system and to accurately measure the out-of-plane spin-signals even in the possible presence of a background charge-signal, we develop a new tool; *Oblique Spin-Valve* (OSV) measurements. For the OSV measurements, we follow a similar measurement procedure as in the SV measurements. However, for the magnetization reversal of FM electrodes, we apply a magnetic field B which makes an angle θ_B with their easy-axes in the y-z plane as shown in Fig. S9(a), instead of applying B_{\parallel} in SV measurements in Fig. 1(a). As a result, the magnetization of the FM electrodes also makes a finite angle θ with its easy axis. In this way, we inject and detect both in-plane and out-of-plane spins in the spin-transport channel. The in-plane magnetic field $\sim B \cos \theta_B$ is responsible for the magnetization switching of C2 and C3 (see details in Supplemental Material). At the event of magnetization reversal at a magnetic field in the OSV measurements, the spin-signal change would appear as a sharp switch in R_{nl} . However, the magnetic field dependent background signal does not change. In this way, in the OSV measurements, we combine the advantages of both SV and the perpendicular-field Hanle measurements, and obtain background-free pure spin-signals.

In an OSV measurement, we measure fractions of both $R_{\text{nl}}^{\parallel}$ and R_{nl}^{\perp} . The OSV spin-signal ΔR_{nl} consists of two components: an in-plane spin-signal component proportional to $R_{\text{nl}}^{\parallel} \cos^2 \theta$ and an out-of-plane spin-signal component proportional to $R_{\text{nl}}^{\perp} \sin^2 \theta$ which get dephased by the applied magnetic field $B \sin \theta_B$ and $B \cos \theta_B$, respectively:

$$\Delta R_{\text{nl}} \simeq R_{\text{nl}}^{\parallel} \cos^2 \theta \zeta_{\parallel}(B \sin \theta_B) + R_{\text{nl}}^{\perp} \sin^2 \theta \zeta_{\perp}(B \cos \theta_B) \quad (2)$$

where $\zeta_{\parallel}(\zeta_{\perp})$ is the functional form for the in-plane (out-of-plane) spin precession dynamics. At larger θ_B , the dephasing of in-plane spin-signal $R_{\text{nl}}^{\parallel}$ is enhanced. Conversely, the dephasing of out-of-plane spin-signal R_{nl}^{\perp} is suppressed. Also, θ increases with θ_B . Therefore, ΔR_{nl} at higher θ_B is dominated by R_{nl}^{\perp} and acquires a similar form as in Eq. 1.

Due to the expected spin-life time anisotropy in BLG/TMD systems and as observed in Hanle measurements in Fig. 3(b), the out-of-plane spin signal magnitude increases with the magnetization angle θ . Similar effect would appear in the OSV measurements at larger θ_B values due to fact that the magnetization switching would occur at larger θ , which would allow to measure a larger fraction of the out-of-plane spin-signal. In order to verify our hypothesis, we first measure the in-plane spin-valve signal $\Delta R_{\text{nl}} = R_{\text{nl}}^{\parallel}$ at $\theta_B = 0^\circ$ for $L = 1 \mu\text{m}$, and then measure R_{nl} at different θ_B values. The mea-

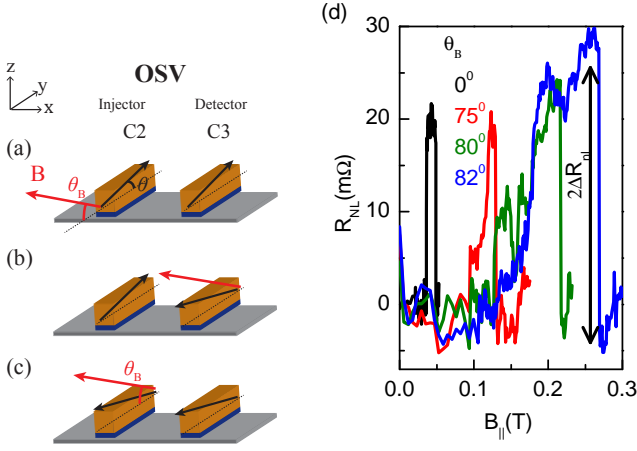


FIG. 4. (a)-(c) Steps for Oblique Spin-valve (OSV) measurements. The magnetization vector for the injector and detector (in black) makes an angle θ with the easy axis and the applied magnetic field B (red vector) for the magnetization reversal remains fixed at an angle θ_B throughout the measurement. The magnetization reversal for the detector and the injector are shown in (b) and (c), respectively. (d) OSV measurements at different θ_B values for the injector-detector separation $L=1 \mu\text{m}$. The OSV spin-signal ΔR_{nl} is defined as half of the magnitude of the switch, labeled with the black arrow. The increase in the spin-valve signal magnitude at higher θ_B confirms the presence of a large spin-relaxation anisotropy. A background signal ($\sim 0.5\text{-}1\Omega$) has been removed from the measured signal for a clear representation (see Supplemental Material for the original measurement).

surement summary is presented in Fig. S9(d). Here, we clearly observe an increase in ΔR_{nl} up to 1.5 times with the increasing θ_B . This result is remarkable in the way that it is possible to observe such clear enhancement even with a small fraction of R_{nl}^\perp , i.e. $\propto R_{nl}^\perp \sin^2 \theta$ contributing to ΔR_{nl} . Note that, following Eq. 2, for $\eta \leq 1$ (or $R_{nl}^\perp \leq R_{nl}^\parallel$), we would never observe an increase in R_{nl} . Therefore the observation of an enhanced signal in the OSV measurements is the confirmation of the present large spin life-time anisotropy in the BLG/WS₂ system.

In order to simplify the analysis and to estimate R_{nl}^\perp from the OSV measurements, we assume that the out-of-plane signal is not significantly affected by the in-plane magnetic field component ($\sim 10 \text{ mT}$) at $\theta_B > 80^\circ$, and $\zeta_\perp(B \cos \theta_B)$ can be omitted from Eq. 2. Note that this assumption would lead to the lower bound of R_{nl}^\perp or τ_\perp . R_{nl}^\parallel and ζ_\parallel are obtained via the in-plane SV and Hanle spin-precession measurements (for details refer to Supplemental Material). From R_{nl}^\perp , we obtain $\lambda_s^\perp \sim 3.7\text{-}4 \mu\text{m}$, which is similar to λ_s^\perp obtained via Hanle measurements, and confirms the validity of the analysis. Using $\lambda_s^\perp = \sqrt{D_s \tau_\perp}$, we estimate $\tau_\perp \sim 1\text{-}2 \text{ ns}$ and the lower limit of $\eta \sim 70$ for V_{bg} between -45 V to 40 V except at $V_{bg} = -20 \text{ V}$ (Fig. S12(a)). Such high magnitude of $\tau_\perp \sim \text{ns}$ is also expected theoretically even in presence of spin-

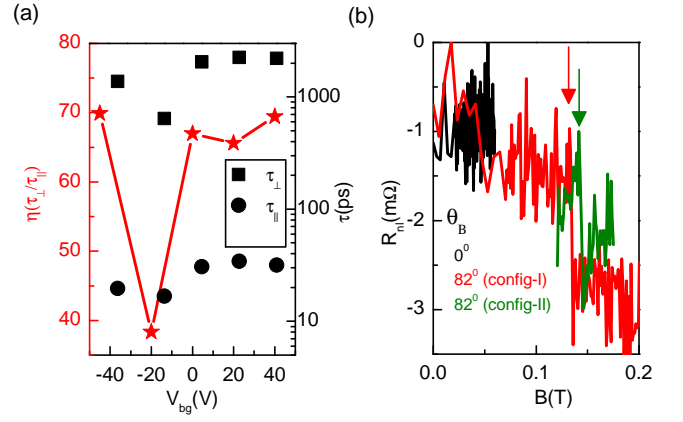


FIG. 5. (a) $\eta - V_{bg}$ plot (in red) on the left y-axis, and respective τ_\parallel and τ_\perp as a function V_{bg} on the right y-axis (b) OSV measurements at $L=4.3 \mu\text{m}$ at $\theta_B = 0^\circ$ (black curve), $\theta_B = 82^\circ$ (config.-I) and for the swapped injector-detector (config.-II) at $\theta_B = 82^\circ$. Arrows in the figure indicate the switching of electrode C2 in Fig. S9

orbit coupling [23], is comparable to the spin relaxation times observed in ultra-clean graphene [5, 42–44], and is a clear signature of strong spin-valley coupling present in the BLG/WS₂ system (see Supplemental Material for additional measurements).

In presence of large η values in BLG/WS₂ heterostructures, the out-of-plane spin-signal can still be detected at larger distances via OSV measurements whereas the in-plane is not even possible to detect. We present such a case in Fig. S12(b) for $L = 4.3 \mu\text{m}$, where no in-plane spin-signal is detected. However, we clearly measure $\Delta R_{nl} = 1.5 \text{ m}\Omega$ for $\theta_B = 82^\circ$, and obtain a similar result by swapping the injector and detector electrodes. The presented measurement unambiguously establishes the fact that indeed due to extremely large η , even though we measure a small fraction $\sim R_{nl}^\perp \sin^2 \theta$ of R_{nl}^\perp , its magnitude is larger than the in-plane spin-signal.

In summary, we report the first spin-transport measurements on a bilayer-graphene/TMD system. We find low in-plane spin relaxation times in the range of 20–40 ps which weakly depend on the carrier density and conductivity of the underlying TMD, and therefore suggest a strong proximity induced spin-orbit coupling in the BLG. Via Hanle and OSV measurements, we electrically inject and detect out-of-plane spins in the BLG/WS₂ system. We estimate the out-of-plane spin relaxation time $\sim 1\text{-}2 \text{ ns}$ and the anisotropy value between 40–70. It is noteworthy that obtained η and τ_\perp for BLG/TMD are much larger compared to previously reported values in Gr/TMD systems in refs. [9, 32]. These results confirm the theoretical prediction that the BLG/TMD systems are highly anisotropic, and show efficient spin-valley coupling for out-of-plane spins. Obtained results unlock the potential of single layer graphene/TMD systems and would be crucial in developing future spintronic devices

such as efficient spin-filters.

We acknowledge J. G. Holstein, H.H. de Vries, T. Schouten and H. Adema for their technical assistance. We thank M.H.D. Guimarães for critically reading the manuscript. This research work was funded by the the Graphene flagship core 1 and core 2 program (grant no. 696656 and 785219), Spinoza Prize (for B.J.v.W.) by the Netherlands Organization for Scientific Research (NWO) and supported by the Zernike Institute for Advanced Materials.

* corresponding author; s.omar@rug.nl

- [1] Z. Wang, D.-K. Ki, J. Y. Khoo, D. Mauro, H. Berger, L. S. Levitov, and A. F. Morpurgo, *Phys. Rev. X* **6**, 041020 (2016).
- [2] M. Gmitra and J. Fabian, *Phys. Rev. B* **92**, 155403 (2015).
- [8] S. Omar and B. J. van Wees, *Phys. Rev. B* **97**, 045414 (2018).
- [4] D. Xiao, W. Yao, and Q. Niu, *Phys. Rev. Lett.* **99**, 236809 (2007).
- [5] J. C. Leutenantsmeyer, J. Ingla-Aynés, J. Fabian, and B. J. van Wees, *Phys. Rev. Lett.* **121**, 127702 (2018).
- [6] J. Xu, T. Zhu, Y. K. Luo, Y.-M. Lu, and R. K. Kawakami, *Phys. Rev. Lett.* **121**, 127703 (2018).
- [9] S. Zihlmann, A. W. Cummings, J. H. Garcia, M. Kedves, K. Watanabe, T. Taniguchi, C. Schönenberger, and P. Makk, *Phys. Rev. B* **97**, 075434 (2018).
- [7] A. W. Cummings, J. H. Garcia, J. Fabian, and S. Roche, *Phys. Rev. Lett.* **119**, 206601 (2017).
- [9] T. S. Ghiasi, J. Ingla-Aynés, A. A. Kaverzin, and B. J. van Wees, *Nano Lett.* **17** (2017).
- [10] C. K. Safeer, J. Ingla-Aynés, F. Herling, J. H. Garcia, M. Vila, N. Ontoso, M. R. Calvo, S. Roche, L. E. Hueso, and F. Casanova, *Nano Lett.* **19**, 1074 (2019).
- [11] J. H. Garcia, A. W. Cummings, and S. Roche, *Nano Lett.* **17**, 5078 (2017).
- [12] Q. Song, H. Zhang, T. Su, W. Yuan, Y. Chen, W. Xing, J. Shi, J. Sun, and W. Han, *Sci. Adv.* **3**, 1602312 (2017).
- [13] A. Soumyanarayanan, N. Reyren, A. Fert, and C. Panagopoulos, *Nature* **539**, 509 (2016).
- [14] M. Isasa, M. C. Martínez-Velarte, E. Villamor, C. Magén, L. Morellón, J. M. De Teresa, M. R. Ibarra, G. Vignale, E. V. Chulkov, E. E. Krasovskii, L. E. Hueso, and F. Casanova, *Phys. Rev. B* **93**, 014420 (2016).
- [15] J. C. R. Sánchez, L. Vila, G. Desfonds, S. Gambarelli, J. P. Attané, J. M. De Teresa, C. Magén, and A. Fert, *Nat. Commun.* **4**, 2944 (2013).
- [16] K. Shen, G. Vignale, and R. Raimondi, *Phys. Rev. Lett.* **112**, 096601 (2014).
- [17] C. L. Kane and E. J. Mele, *Phys. Rev. Lett.* **95**, 146802 (2005).
- [18] B. Yang, M.-F. Tu, J. Kim, Y. Wu, H. Wang, J. Alicea, R. Wu, M. Bockrath, and J. Shi, *2D Mater.* **3**, 031012 (2016).
- [19] T. Frank, P. Högl, M. Gmitra, D. Kochan, and J. Fabian, *Phys. Rev. Lett.* **120**, 156402 (2018).
- [20] L. Du, Q. Zhang, B. Gong, M. Liao, J. Zhu, H. Yu, R. He, K. Liu, R. Yang, D. Shi, L. Gu, F. Yan, G. Zhang, and Q. Zhang, *Phys. Rev. B* **97**, 115445 (2018).
- [21] J. O. Island, X. Cui, C. Lewandowski, J. Y. Khoo, E. M. Spanton, H. Zhou, D. Rhodes, J. C. Hone, T. Taniguchi, K. Watanabe, L. S. Levitov, M. P. Zaletel, and A. F. Young, *Nature*, **1** (2019).
- [22] J. Y. Khoo, A. F. Morpurgo, and L. Levitov, *Nano Lett.* **17**, 7003 (2017).
- [23] M. Gmitra and J. Fabian, *Phys. Rev. Lett.* **119**, 146401 (2017).
- [24] A. M. Afzal, M. F. Khan, G. Nazir, G. Dastgeer, S. Aftab, I. Akhtar, Y. Seo, and J. Eom, *Sci. Rep.* **8**, 3412 (2018).
- [25] P. Ye, R. Y. Yuan, X. Zhao, and Y. Guo, *J. Appl. Phys.* **121**, 144302 (2017).
- [4] S. Omar and B. J. van Wees, *Phys. Rev. B* **95**, 081404(R) (2017).
- [27] M. Offidani, M. Milletari, R. Raimondi, and A. Ferreira, *Phys. Rev. Lett.* **119**, 196801 (2017).
- [28] C. Huang, Y.D. Chong, and M. A. Cazalilla, *Phys. Rev. Lett.* **119**, 136804 (2017).
- [29] Y. Ando and M. Shiraishi, *J. Phys. Soc. Jpn.* **86**, 011001 (2016).
- [30] M. Gurram, S. Omar, and B. J. van Wees, *2D Mater.* **5**, 032004 (2018).
- [31] Z. Wang, D.-K. Ki, H. Chen, H. Berger, A. H. MacDonald, and A. F. Morpurgo, *Nat. Commun.* **6**, 9339 (2015).
- [32] L. A. Benítez, J. F. Sierra, W. S. Torres, A. Arrighi, F. Bonell, M. V. Costache, and S. O. Valenzuela, *Nat. Phys.* **14**, 303 (2018).
- [33] T. Zhu and R. K. Kawakami, *Phys. Rev. B* **97**, 144413 (2018).
- [34] N. Tombros, S. Tanabe, A. Veligura, C. Józsa, M. Popinciuc, H. T. Jonkman, and B. J. van Wees, *Phys. Rev. Lett.* **101**, 046601 (2008).
- [35] M. Popinciuc, C. Józsa, P. J. Zomer, N. Tombros, A. Veligura, H. T. Jonkman, and B. J. van Wees, *Phys. Rev. B* **80**, 214427 (2009).
- [36] M.H.D. Guimarães, P.J. Zomer, J. Ingla-Aynés, J.C. Brant, N. Tombros, and B.J. van Wees, *Phys. Rev. Lett.* **113**, 086602 (2014).
- [37] A. Avsar, D. Unuchek, J. Liu, O. L. Sanchez, K. Watanabe, T. Taniguchi, B. Özyilmaz, and A. Kis, *ACS Nano* **11**, 11678 (2017).
- [38] Y. K. Luo, J. Xu, T. Zhu, G. Wu, E. J. McCormick, W. Zhan, M. R. Neupane, and R. K. Kawakami, *Nano Lett.* **17**, 3877 (2017).
- [2] P. J. Zomer, M. H. D. Guimarães, J. C. Brant, N. Tombros, and B. J. van Wees, *Appl. Phys. Lett.* **105**, 013101 (2014).
- [40] W. Yan, O. Txoperena, R. Llopis, H. Dery, L. E. Hueso, and F. Casanova, *Nat. Commun.* **7**, 13372 (2016).
- [41] A. Dankert and S. P. Dash, *Nat. Commun.* **8**, 16093 (2017).
- [42] M. Gurram, S. Omar, and B. J. van Wees, *Nat. Commun.* **8**, 248 (2017).
- [43] J. Ingla-Aynés, M. H. D. Guimarães, R. J. Meijerink, P. J. Zomer, and B. J. van Wees, *Phys. Rev. B* **92**, 201410(R) (2015).
- [44] M. Drögele, C. Franzen, F. Volmer, T. Pohlmann, L. Banszerus, M. Wolter, K. Watanabe, T. Taniguchi, C. Stampfer, and B. Beschoten, *Nano Lett.* **16**, 3533 (2016).

Supplementary Information

SAMPLE PREPARATION

Tungsten disulfide (WS_2) flakes are exfoliated on a polydimethylsiloxane (PDMS) stamp and identified using an optical microscope. The desired flake is transferred onto a pre-cleaned SiO_2/Si substrate ($t_{\text{SiO}_2}=500$ nm), using a transfer-stage. The transferred flake on SiO_2 is annealed in an Ar- H_2 environment at 240°C for 6 hours in order to achieve a clean top-interface of WS_2 , to be contacted with graphene. The graphene flake is exfoliated from a ZYB grade HOPG (Highly oriented pyrolytic graphite) crystal and boron nitride (BN) is exfoliated from BN crystals (size ~ 1 mm) onto different SiO_2/Si substrates ($t_{\text{SiO}_2}=90$ nm). Both crystals were obtained from HQ Graphene. The desired bilayer-graphene (BLG) flakes are identified via their optical contrast using an optical microscope. Boron-nitride flakes are identified via the optical microscope. The thickness of hBN and WS_2 flakes is determined via Atomic Force Microscopy. In order to prepare an hBN/Gr/ WS_2 stack, we use a polycarbonate (PC) film attached to a PDMS stamp as a sacrificial layer. Finally, the stack is annealed again in the Ar- H_2 environment for six hours at 235°C to remove the remaining PC polymer residues.

In order to define contacts, a poly-methyl methacrylate (PMMA) solution is spin-coated over the stack and the contacts are defined via the electron-beam lithography (EBL). The PMMA polymer exposed via the electron beam gets dissolved in a MIBK:IPA (1:3) solution. In the next step, 0.7 nm Al is deposited in two steps, each step of 0.35 nm followed by 12 minutes oxidation in the oxygen rich environment to form a AlO_x tunnel barrier. On top of it, 65 nm thick cobalt (Co) is deposited to form the ferromagnetic (FM) tunnel contacts with a 3 nm thick Al capping layer to prevent the oxidation of Co electrodes. The residual metal on the polymer is removed by the lift-off process in acetone solution at 40°C .

CHARGE TRANSPORT MEASUREMENTS

Graphene

We measure the charge transport in graphene via the four-probe local measurement scheme. For measuring the gate-dependent resistance of graphene-on- WS_2 , a fixed ac current $i_{\text{ac}} \sim 100$ nA is applied between contacts C1-C4 and the voltage-drop is measured between contacts C2-C3 (Fig. S1(a)), while the back-gate voltage is swept. The maximum resistance point in the Dirac curve is denoted as the charge neutrality point (CNP). For graphene-on- WS_2 , it is possible to tune the Fermi energy E_F and the carrier-density in graphene only when E_F lies

only in the band-gap of WS_2 . Since, we do not observe any saturation in the resistance of the BLG (red curve Fig. S2(a)), we probe the charge/ spin transport where the Fermi level lies within the band gap of WS_2 . The CNP cannot be accessed within the applied V_{bg} range. However, it is possible to access the CNP and the hole doped regime (black curves Fig. S2(a)) in the region underneath the top-hBN flake, outlined as red region in the optical image in Fig. S1(b), using the top-gate application due to its higher capacitance. In order to extract the carrier mobility μ , we fit the charge-conductivity σ versus carrier density n plot with the following equation:

$$\sigma = \frac{1}{R_{\text{sq}}} = \frac{ne\mu + \sigma_0}{1 + R_s(ne\mu + \sigma_0)}. \quad (\text{S1})$$

Here R_{sq} is the square resistance of graphene, σ_0 is the conductivity at the CNP, R_s is the residual resistance due to short-range scattering [1, 2] and e is the electronic charge. We fit the $\sigma - n$ data for n (both electrons and holes) in the range $0.5\text{-}2.5 \times 10^{12} \text{ cm}^{-2}$ with Eq. S1. For the encapsulated region we obtain the electron-mobility $\mu_e \sim 3,000 \text{ cm}^2\text{V}^{-1}\text{s}^{-1}$ for stack A. For stack B, we could not access the CNP within the applied V_{bg} range due to heavily n-doped BLG. Therefore, we could not extract the mobility.

Tungsten disulfide (WS_2)

In order to obtain the transfer characteristics, i.e. back-gate dependent conductivity of the WS_2 substrate, we apply a dc voltage $V_{\text{DS}} = 0.2$ V and measured the current I_{DS} between the top gate contact, that touches the bottom WS_2 at point D and a contact S on the BLG flake (Fig. S1(b)), and vary the back-gate voltage V_{bg} in order to change the resistivity of WS_2 . The $I_{\text{DS}} - V_{\text{bg}}$ behavior of the bottom- WS_2 flake of stack A is plotted in Fig. S3.

SPIN TRANSPORT MEASUREMENTS

For spin-valve (SV) measurements, a charge current i_{ac} is applied between contacts C2-C1 and a nonlocal voltage v_{nl} is measured between C3-C4 (Fig. S1(a)). First an in-plane magnetic field $B_{\parallel} \sim 0.2$ T is applied along the easy axes of the ferromagnetic (FM) electrodes (+y-axis), in order to align their magnetization along the field. Now, B_{\parallel} is swept in the opposite direction (-y-axis) and the FM contacts reverse their magnetization direction along the applied field, one at a time. This magnetization reversal appears as a sharp transition in v_{nl} or in the nonlocal resistance $R_{\text{nl}} = v_{\text{nl}}/i_{\text{ac}}$. The spin-signal is $R_{\text{nl}}^{\parallel} = \frac{R_{\text{nl}}^{\text{P}} - R_{\text{nl}}^{\text{AP}}}{2}$, where $R_{\text{nl}}^{\text{P(AP)}}$ represents the R_{nl} value of the two level spin-valve signal, corresponding to the

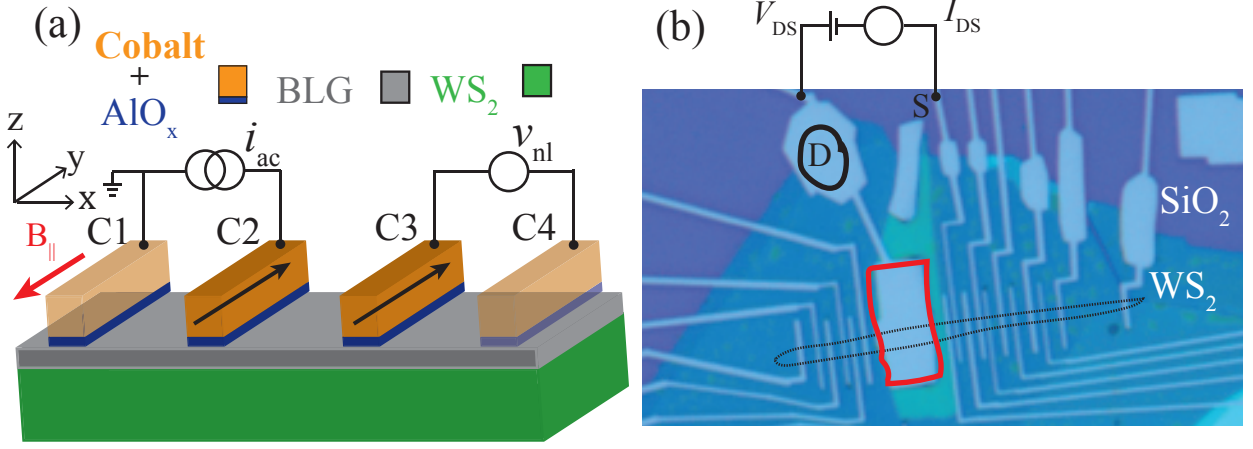


FIG. S1. (a) Nonlocal spin-transport measurement scheme. (b) An optical micrograph of a fabricated WS₂/BLG/hBN stack (stack A). BLG is outlined with black dashed lines and hBN top-gate is outlined in red.

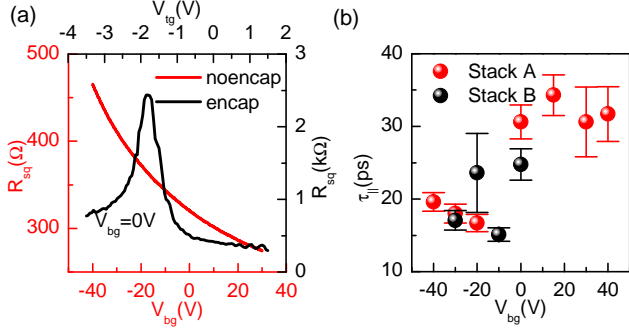


FIG. S2. (a) $R_{sq} - V_{bg}(t_g)$ dependence for the nonencapsulated (encapsulated) region is shown on the left (right) axis (red(black) curves) for stack A. (b) $\tau_{||} - V_{bg}$ for BLG/WS₂

parallel (P) and anti-parallel (AP) magnetization of the FM electrodes. In the nonlocal measurement geometry the spin-signal $R_{nl}^{||}$ is given by:

$$R_{nl}^{||} = \frac{P^2 R_{sq} \lambda_s^{||} e^{-\frac{L}{\lambda_s^{||}}}}{2w}. \quad (S2)$$

Here $\lambda_s^{||}$ is the spin-relaxation length for the in-plane spins in graphene and P is the contact polarization of injector and detector electrodes for in-plane spins, R_{sq} is the graphene sheet-resistance and w is the width of spin-transport channel.

For Hanle spin-precession measurements, for a fixed P (AP) configuration, an out-of-plane magnetic field B_{\perp} is applied and the injected in-plane spin-accumulation precesses around the applied field. From these measurements, we obtain the spin diffusion coefficient D_s and in-plane spin-relaxation time $\tau_{||}$, and estimate the spin-relaxation length $\lambda_s^{||} = \sqrt{D_s \tau_{||}}$. Using this $\lambda_s^{||}$ in Eq. S2,

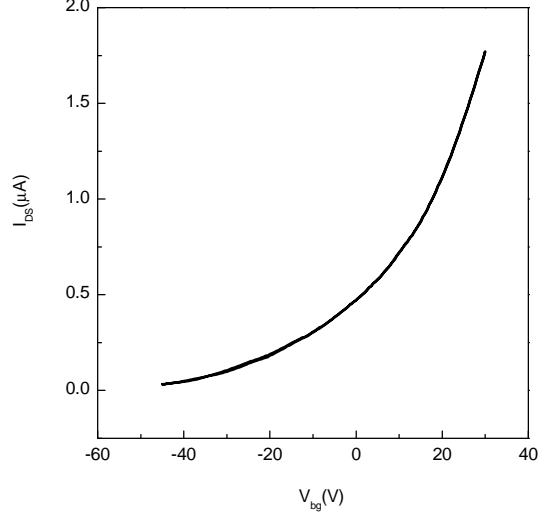


FIG. S3. $I_{DS} - V_{bg}$ behavior of the bottom-WS₂ flake of stack A at $V_{DS} = 0.2$ V applied between the top-gate electrode and another electrode contacting the BLG-on-WS₂. The measurement scheme is shown in Fig. S1(b).

we obtain the contact polarization $P \sim 3-5$ % for in-plane spin-transport. We would like to make a remark here that some of the contacts in stack A have the opposite (i.e., negative) sign of P for in-plane spin-transport. The origin of the negative sign is nontrivial and possibly could be due to the specific nature of the FM tunnel barrier interface with the graphene-on-TMD.

SV measurements as a function of V_{bg} (stack B) are summarized in Figs. S4 and S5 for stack A and stack B, respectively. For both samples, there is no significant

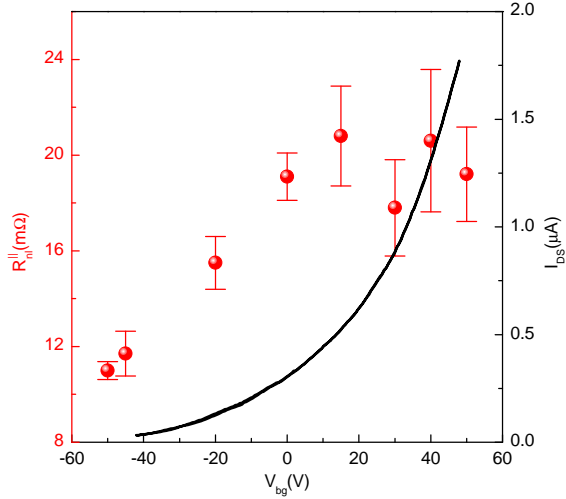


FIG. S4. In-plane Spin valve (SV) measurements for stack A as a function of V_{bg} and the conductance of the underlying TMD (WS_2).

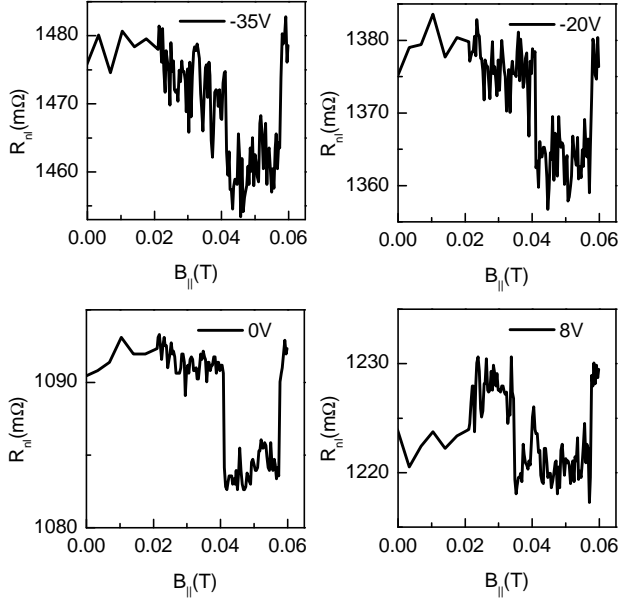


FIG. S5. In-plane Spin valve (SV) measurements for stack B at different back-gate voltage (V_{bg}) values. $R_{ni}^||$ does not change with V_{bg} , indicating that the spin-absorption is not the dominant mechanism for spin-relaxation within the applied V_{bg} range.

change in the spin-signal within the range $\Delta V_{bg} \sim \pm 40V$. For stack A, the FM contacts have low resistance ($\leq 1k\Omega$) and this is the reason that there is a modest

increase in $R_{ni}^||$ at higher charge carrier density due to the suppressed contact-induced spin-relaxation [3, 4]. Both measurements do not exhibit any measurable signature of spin-absorption due to the conductivity modulation of the underlying TMD substrate.

GENERALIZED STONER-WOHLFARTH MODEL FOR EXTRACTING MAGNETIZATION ANGLE

In this section, we describe the basics of Stoner-Wohlfarth (SW) model, and extend it for three-dimensional case in order to extract the magnetization-direction of a bar-magnet in presence of an external magnetic field.

The total energy E_T of a ferromagnet in a magnetic field is expressed as:

$$E_T = E_A + E_Z, \quad (S3)$$

where E_Z and E_A are the contributions from Zeeman and anisotropic energy, respectively.

First a magnetic field B is applied which makes an angle ϕ_B with the x-axis and an angle θ_B (Fig. S6(b)), having its components B_x, B_y, B_z along x, y and z axes, respectively. Here B can be parameterized with respect to θ_B, ϕ_B in the following way:

$$B_x = B \cos \theta_B \cos \phi_B, B_y = B \cos \theta_B \sin \phi_B, B_z = B \sin \theta_B. \quad (S4)$$

For a ferromagnetic bar with its anisotropic constants K_x, K_y and K_z along x, y and z axis, respectively, and \vec{M} making an angle α_x, α_y and α_z with the x, y and z axis, respectively, E_T be generalized to a three-dimensional form as:

$$E_T = \sum_{i=x,y,z} E_A^i + \sum_{i=x,y,z} E_Z^i \quad (S5)$$

Now we write down the expression for E_A^i and E_Z^i which have contributions from M_i and B_i .

At (B, θ_B, ϕ_B) \vec{M} makes the azimuthal angle ϕ with the x-axis in the x-y plane and polar angle θ with the y-axis in the y-z plane (Fig. S6(c)). Therefore, $\vec{M} = (M_x, M_y, M_z) = (M \cos \theta \cos \phi, M \cos \theta \sin \phi, M \sin \theta)$. The anisotropic and Zeeman energy terms can again be parameterized with respect to $\theta, \phi, \theta_B, \phi_B$ in to a three-dimensional form:

$$\begin{aligned} E_A^x &= K_x \sin^2 \alpha_x = K_x (1 - \cos^2 \theta \cos^2 \phi), \\ E_A^y &= K_y \sin^2 \alpha_y = K_y (1 - \cos^2 \theta \sin^2 \phi), \\ E_A^z &= K_z \sin^2 \alpha_z = K_z \cos^2 \theta, \end{aligned} \quad (S6)$$

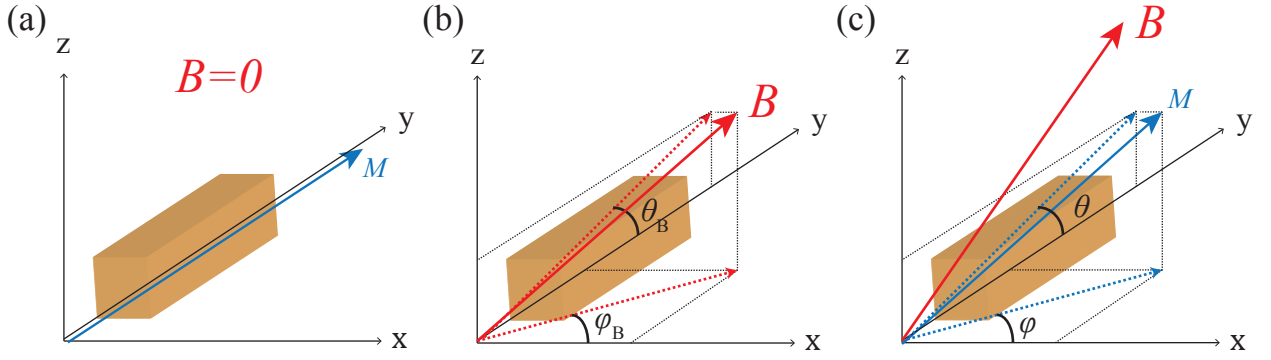


FIG. S6. Easy axis of magnetization M for the bar magnet is along its length, i.e. along y -axis. (a) M is along y -axis for $B = 0$ or when B is applied along y -axis. (b) For $B \neq 0$, M makes an angle θ with the x - y plane and angle ϕ with the y - z plane and (c) B makes an angle θ_B with the x - y plane and angle ϕ_B with the y - z plane.

and

$$\begin{aligned} E_z^x &= -M_x B_x, \\ E_z^y &= -M_y B_y, \\ E_z^z &= -M_z B_z. \end{aligned} \quad (\text{S7})$$

Now the expressions in Eq.s S6 and S7 can be substituted to Eq. S5 and a full functional form of E_T can be obtained.

In order to obtain (θ, ϕ) which correspond to $\min(E_T)$, we solve for the global energy minima of Eq. S5 by imposing two following conditions:

$$\begin{aligned} \frac{\partial E_T(\theta, \phi)}{\partial \theta} &= \frac{\partial E_T(\theta, \phi)}{\partial \phi} = 0, \\ \frac{\partial^2 E_T(\theta, \phi)}{\partial \theta^2} &= \frac{\partial^2 E_T(\theta, \phi)}{\partial \phi^2} = 0. \end{aligned} \quad (\text{S8})$$

Since \vec{M} has its easy axis along y -axis, $K_y = 0$. We use $M_{\text{cobalt}} = 5 \times 10^5 \text{ A/m}$ as reported in literature [5]. In order to obtain K_z , we use the saturation magnetic field M_s of the FM electrodes along z -direction, i.e. $\sim 1.5 \text{ T}$ for the thickness (65nm) of the FM electrodes, and use the relation $M_s = \frac{2K_z}{M_{\text{cobalt}}}$ [6]. In order to obtain K_x , we use the in-plane switching fields of FM electrodes, and use them as the only free parameter in the model to obtain the in-plane magnetization switching as obtained in measurements.

Using the procedure, we numerically solve for θ, ϕ for different directions of the applied magnetic field with respect to the minimum energy constraint in Eq. S8 using MATLAB. The simulation outcome is shown in Fig. S7.

OBLIQUE SPIN-VALVE MEASUREMENTS

Before starting the Oblique Spin-valve (OSV) measurements, we set the initial \vec{M} of the FM electrodes along

$+y$ -axis, i.e. along their easy magnetization-axis. Here, the measured spin-signal $R_{\text{nl}}^T = R_{\text{nl}}^{\parallel}$.

Step-I: We apply a magnetic field B in the opposite direction which makes an angle θ_B with the $-y$ -axis, as shown in Fig. S8(a). Here, we assume that both injector and the detector due to their identical thickness have the same out-of-plane anisotropy value K_z . As the magnitude of B increases, the magnetization \vec{M} of both injector and detector FM electrodes makes a finite angle θ_i with respect to its initial direction ($+y$ -axis), and the injected spins have their quantization axis along θ_i (Fig. S8(a)). Now, the measured spin-signal $R_{\text{nl}}^{\text{P1}}$ in the parallel configuration can be expressed as:

$$R_{\text{nl}}^{\text{P1}} = R_{\text{nl}}^{\parallel} \cos^2 \theta_i \zeta_{\parallel}(B \sin \theta_B) + R_{\text{nl}}^{\perp} \sin^2 \theta_i \zeta_{\perp}(B \cos \theta_B) \quad (\text{S9})$$

Here, $\zeta_{\parallel(\perp)}$ is the functional form for the in-plane (out-of-plane) spin precession of dynamics.

Step-II: Due to different widths of the FM electrodes, they have different in-plane anisotropies and different switching fields. At a certain magnetic field, the magnetization of the detector reverses the direction of its y -component. Now, the detector magnetization subtends an angle θ_f with the negative y -axis (Fig. S8(b)). This activity is seen as a switch due to the direction reversal of both in-plane and out-of-plane magnetization component with respect to its initial orientation. The factorization of in-plane and out-of-plane components can be understood via the presented vector diagram in Fig. S8(b) in following steps:

- The injector electrode injects the spin signal along θ_i , represented by the blue arrow b-c in Fig. S8(b).
- The detector measures the projection of the injected spin-signal which has its quantization axis at θ_i , along the detector magnetization axis along b-a, shown as a black dashed line in Fig. S8(b). Now the magnetization axis, along which the spin-signal

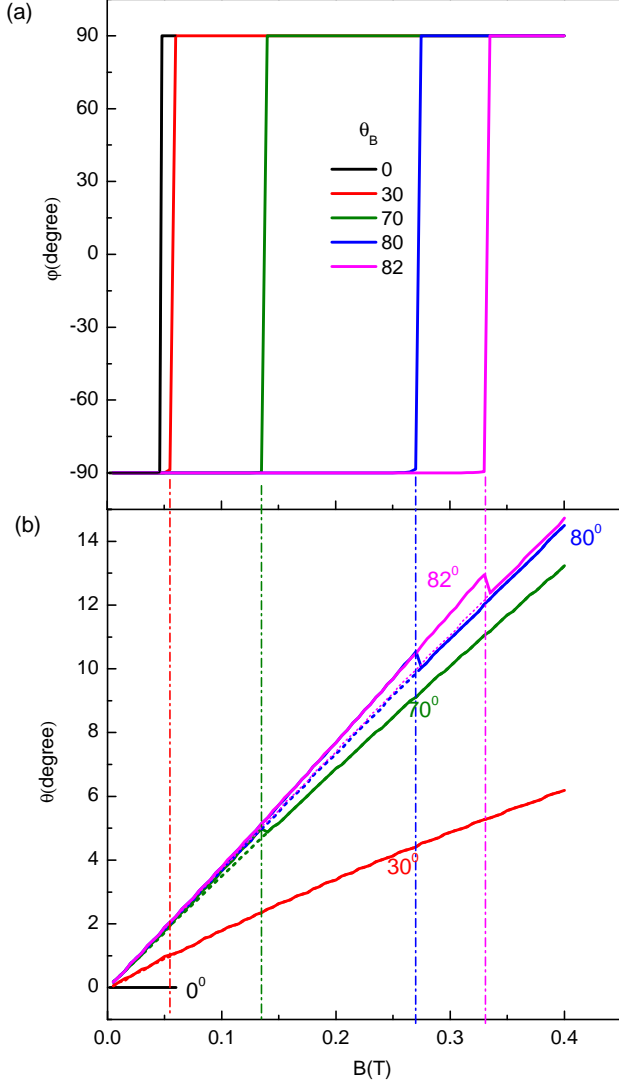


FIG. S7. (a) in-plane ϕ and (b) out-of-plane θ angles as a function of magnetic field at different θ_B values. Dashed lines in the $\theta - B$ plot correspond to the situation when B and M have their in-plane components in the same direction in the y - z plane. Sharp switches in ϕ, θ correspond to the event when the magnetization reversal occurs.

is measured becomes:

$$\vec{M}_{\text{injector}}^{\text{new}} = -(\cos \theta_f \hat{j} + \sin \theta_f \hat{k}) \cos(\theta_i + \theta_f), \quad (\text{S10})$$

where \hat{j}, \hat{k} are the unit vectors along y and z -axis, respectively. Since the in-plane and out-of-plane spin-signals have magnitudes $R_{\text{nl}}^{\parallel} \cos \theta_i \zeta_{\parallel} (B \sin \theta_B)$ and $R_{\text{nl}}^{\perp} \sin \theta_i \zeta_{\perp} (B \cos \theta_B)$, the spin-signal measured by the detector becomes:

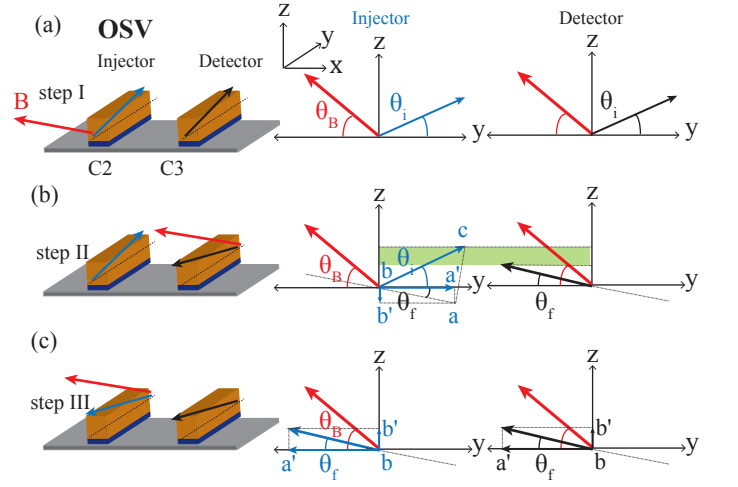


FIG. S8. Steps for Oblique Spin Valve Measurements

$$R_{\text{nl}}^{\text{AP}} = -[R_{\text{nl}}^{\parallel} \cos \theta_i \zeta_{\parallel} (B \sin \theta_B) \cos \theta_f + R_{\text{nl}}^{\perp} \sin \theta_i \zeta_{\perp} (B \cos \theta_B) \sin \theta_f] \cos(\theta_i + \theta_f) \quad (\text{S11})$$

Step-III: Finally, the injector electrode reverses its magnetization and both electrodes have their magnetizations pointing in the same direction, and making an angle θ_f with the device plane Fig. S8(c). The spin-signal $R_{\text{nl}}^{\text{AP}}$ has the same expression as in Eq. S9, except θ_i is replaced with θ_f . The desired spin valve signal can be obtained by subtracting Eq. S11 with Eq. S9 with appropriate θ values, obtained from Fig. S7 at corresponding magnetization switching fields.

A data set for the oblique spin valve measurements is shown in Fig. S9. As expected by the simulation results in Fig. S7, the magnetization switching follows the relation $B_0 \sim B \cos \theta_B$, where B_0 is the magnetization switching field ~ 40 mT for the in-plane spin valve (black curve in Fig. S9). The measured signal has contribution from both in-plane and out-of-plane magnetization switching. As suggested by the simulation results, the magnetic field dependent background in the measurement has similar trend as observed in Fig. S7(b) due to the field-dependent magnetization angle, and has contribution of the out-of-plane spin-signal. The processed data after removing this field dependence is shown in Fig.3(a) of the main text which shows a clear enhancement in the measured spin valve signal magnitude. This is a consequence of large spin-life time anisotropy present in the system, and is discussed in the manuscript in detail.

An additional set of OSV measurements for a different region (on the right side) of stack A is shown in Fig. S10. For this set the FM electrodes at $\theta_B = 83^\circ$ switch earlier than the expected switching field, i.e. $B_0/\cos \theta_b \sim 300$ mT, and using the angles obtained in Fig. S7 and τ_{\parallel} in

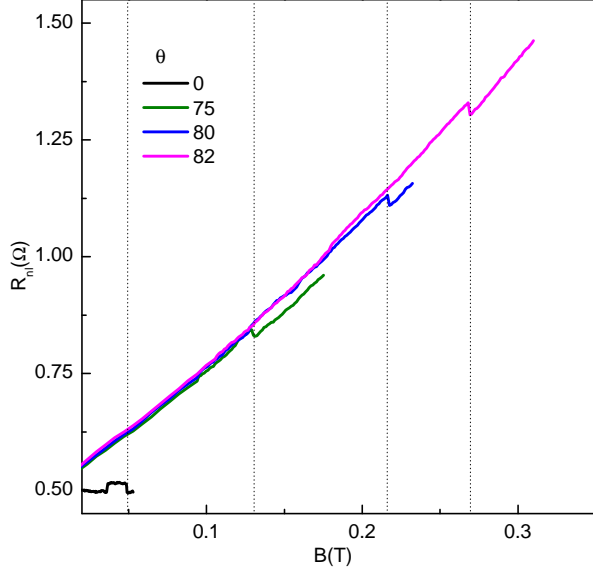


FIG. S9. (a) OSV measurements for BLG/WS₂ at different θ_B values for the injector-detector separation $L=1 \mu\text{m}$ with out background removal. Vertical dashed lines indicate the magnitudes of the magnetization switching field magnitudes on x-axis at different θ_B values. The black curve is the in-plane spin-valve measurement at $\theta_B = 0^\circ$. The curves measured at $\theta_B = 75 - 82^\circ$ have the contribution from both in-plane and out-of-plane spin-signals. The enhanced contribution of the out-of-plane spin-signal component during the magnetization reversal, i.e. enhanced switch magnitude in R_{nl} for the measurements at higher θ_B values can be seen clearly in Fig. 4(b) of the main text after the background removal.

the region, the analysis yields $\eta \sim 244$ and $\tau_\perp \sim 4$ ns. The overestimation of η is probably due to earlier switching of the FM electrode. However, the effect of anisotropy can be clearly seen in the measurement.

NONLOCAL HANLE SIGNAL VERSUS ORBITAL MAGNETORESISTANCE

A negligible charge background signal due to the orbital magnetoresistance of the graphene flake is present at the applied $B_\perp = 0$ (Fig. S11). Here, for the same channel R_{nl} increases almost 50 fold whereas there is hardly any change in the background MR signal (Fig. S11). Therefore the observed increase in R_{nl} at high B_\perp is clearly not due to the orbital magnetoresistance of the graphene-flake.

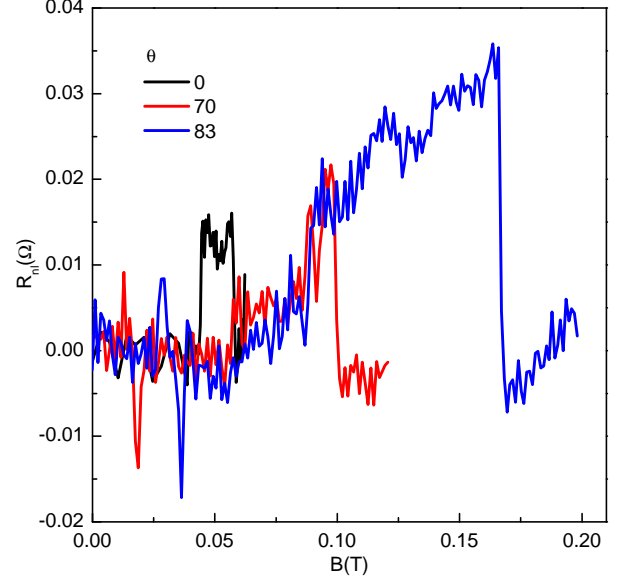


FIG. S10. Additional OSV measurements at $L=1 \mu\text{m}$ at $V_{bg} = 0$ V (stack A).

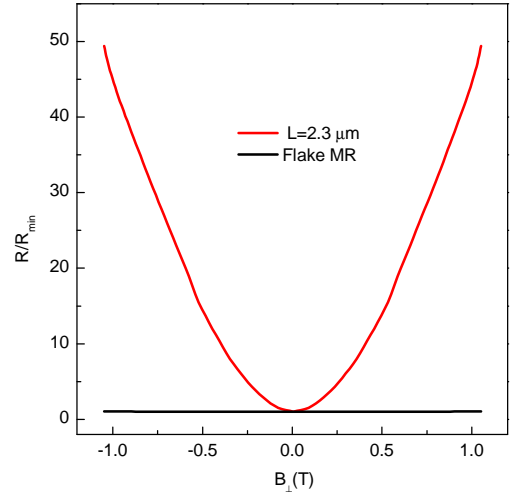


FIG. S11. Hanle (parallel configuration) at the injector-detector separation $L = 2.3 \mu\text{m}$ and the flake magnetoresistance (black curve) are symmetrized and normalized with R_{nl}^{min} and $R_{\text{MR}}^{\text{min}}$ value in order to emphasize the signal enhancement in the nonlocal configuration.

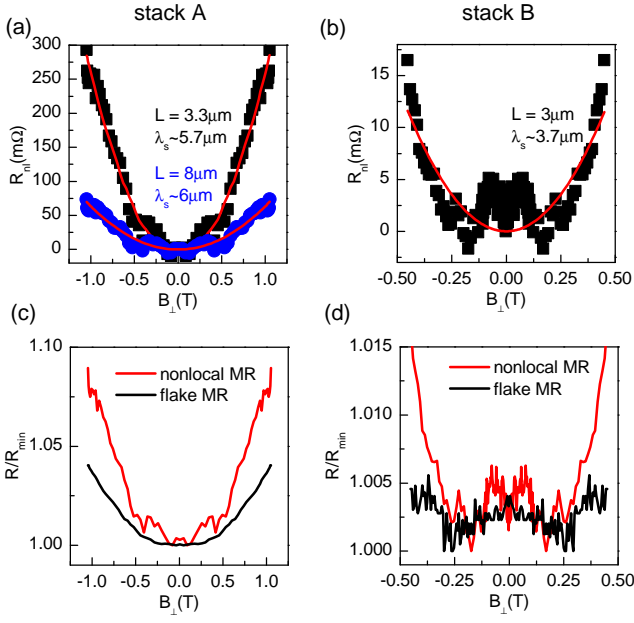


FIG. S12. (a) Symmetrized Hanle curves (stack A) and fits (in red) with Eq. S18 after subtracting the background-signal of $\sim 3 \Omega$ and 1Ω at two different injector-detector separations, respectively (at $V_{bg} = 0$) result in similar λ_s^{\perp} (b) Additional Hanle measurements and the fit for stack B (after subtracting the background signal $\sim 1 \Omega$). Nonlocal resistance and flake magnetoresistance are normalized and plotted together in order to highlight the relative difference between them in (c) for stack A and (d) for stack B.

ESTIMATING OUT-OF-PLANE SPIN RELAXATION TIME VIA HANLE MEASUREMENTS

It is already explained in the previous section that at a nonzero magnetic field B applied at an angle θ_B with the device plane, the magnetization vector \vec{M} makes a finite angle θ with the device plane (Fig. S6). Here, we represent a specific case with $\theta_B = 90^\circ$ for Hanle measurements. Here, we would represent B as B_{\perp} and assume that both injector and detector behave identically and their \vec{M} vectors make same angle θ . At $B_{\perp} \neq 0$, \vec{M} has its quatization axis not in the device plane, it also electrically injects a nonzero out-of-plane spin-signal. If \vec{M} for both injector and detector were pointing perpendicular to the device plane, the measured nonlocal signal R_{nl}^{\perp} would be written as:

$$R_{nl}^{\perp} = \frac{P^2 R_{sq}(B_{\perp}) \lambda_s^{\perp} e^{-\frac{L}{\lambda_s^{\perp}}}}{2w}. \quad (S12)$$

Here λ_s^{\perp} is the spin-relaxation length for the out-of-plane spins in graphene and P is the contact polarization of injector and detector electrodes, which is obtained via in-plane spin-transport measurements. $R_{sq}(B_{\perp})$ is the

magnetoresistance (MR) of the graphene flake in presence of the out-of-plane magnetic field. However, in general $\theta < \pi/2$ for the values of $B_{\perp} < 1.2$ T due to limitations of the electromagnet in the setup, we inject and detect only a fraction of R_{nl}^{\perp} that is proportional to $\sin^2 \theta(B_{\perp})$, and the in-plane spin-signal R_{nl}^{\parallel} that is proportional to $\cos^2 \theta(B_{\perp})$ and gets dephased by B_{\perp} .

FM contacts also measure charge-related MR and a constant spin-independent background due to current spreading and homogeneous current distribution even in the nonlocal part of the circuit. This contribution can be represented as:

$$R_{nl}^{ch} = C1 R_{sq}(B_{\perp}) + C2 \quad (S13)$$

Therefore, the total measured nonlocal signal R_{nl}^T is:

$$R_{nl}^T(B_{\perp}) = R_{nl}^{\perp} \sin^2 \theta(B_{\perp}) \pm R_{nl}^{\parallel} \cos^2 \theta(B_{\perp}) \times \zeta(B_{\perp}) + R_{nl}^{ch} \quad (S14)$$

Here \pm before the expression for the in-plane spin signal is for P(AP) magnetization configuration of the injector-detector electrodes and $\zeta(B_{\perp})$ is the expression for Hanle precession dynamics. The second term can be omitted from Eq. S14 by measuring $R_{nl}^T(B_{\perp})$ for both P and AP configurations of FM electrodes and then averaging them out. Via this exercise, we get rid of the in-plane spin signal and get the following expression:

$$R_{nl}^T(B_{\perp}) = R_{nl}^{\perp} \sin^2 \theta(B_{\perp}) + C1 R_{sq}(B_{\perp}) + C2 \quad (S15)$$

At $B_{\perp} = 0$ T, $R_{sq}(B_{\perp} = 0) = R_{sq}$ and $\theta(B_{\perp} = 0) = 0$, Eq. S15 reduces to:

$$R_{nl}^T(0) = C1 R_{sq} + C2 \quad (S16)$$

By subtracting Eq. S16 to Eq. S15 and dividing the resulting expression with $R_{sq}(B_{\perp})$, we obtain:

$$\frac{R_{nl}^T(B_{\perp}) - R_{nl}^T(0)}{R_{sq}(B_{\perp})} = \frac{R_{nl}^{\perp} \sin^2 \theta(B_{\perp})}{R_{sq}(B_{\perp})} + C1 \frac{R_{sq}(B_{\perp}) - R_{sq}}{R_{sq}(B_{\perp})} \quad (S17)$$

Using Eq. S12, we obtain the final expression:

$$\frac{R_{nl}^T(B_{\perp}) - R_{nl}^T(0)}{R_{sq}(B_{\perp})} = \frac{p^2 \lambda_s^{\perp} e^{-\frac{L}{\lambda_s^{\perp}}} \sin^2 \theta(B_{\perp})}{2w} + C1 \frac{R_{sq}(B_{\perp}) - R_{sq}}{R_{sq}(B_{\perp})}, \quad (S18)$$

and use it for extracting λ_s^{\perp} and the constant $C1$ which is the fraction of flake MR contributing to the nonlocal signal. Here, θ is obtained via simulations, following the procedure mentioned earlier using $\theta_B = \pi/2$. Experimental data of R_{nl} and the fit with Eq. S18 is shown in Fig. S12(a,b).

ESTIMATION OF VALLEY-ZEEMAN AND RASHBA SOC STRENGTHS

In graphene/TMD heterostructures, different spin-orbit coupling strengths are induced in graphene in the in-plane and out-of-plane directions because of weak van der Waals interactions with the contacting TMD [7]. This effect can be measured in the anisotropy of in-plane (τ_{\parallel}) and out-of-plane spin-relaxation time (τ_{\perp}) using the following relation:

$$\eta = \frac{\tau_{\perp}}{\tau_{\parallel}} \sim \left(\frac{\lambda_{VZ}}{\lambda_R} \right)^2 \frac{\tau_{iV}}{\tau_p}. \quad (\text{S19})$$

Here λ_{VZ} and λ_R are spin-orbit coupling strengths corresponding to the out-of-plane and in-plane spin-orbit field, respectively. τ_{iV} is the intervalley scattering time, and τ_p is the momentum relaxation time of electron.

From the charge and spin transport measurements, we obtain the diffusion coefficient $D \sim 0.01\text{-}0.03 \text{ m}^2\text{V}^{-1}\text{s}^{-1}$. Following the relation $D \sim v_F^2 \tau_p$, where $v_F = 10^6 \text{ m/s}$ is the Fermi velocity of electrons in graphene, we obtain $\tau_p \sim 0.01\text{-}0.03 \text{ ps}$. Typically, for strong intervalley scattering, we can assume the relation $\tau_{iV} \sim 5\tau_p$ [7], and estimate $\tau_{iV} \sim 0.05\text{-}0.15 \text{ ps}$. From the spin-transport experiments, we already know $\tau_{\perp} \sim 1 \text{ ns}$ and $\tau_{\parallel} \sim 30 \text{ ps}$. We can now estimate λ_R and λ_{VZ} independently by assuming that the spin-relaxation is dominated by the Dyakonov Perel mechanism [7], i.e. using the relations

$\tau_{\perp}^{-1} = (2\lambda_R/\hbar)^2 \tau_p$ and $\tau_{\parallel}^{-1} = (2\lambda_{VZ}/\hbar)^2 \tau_{iV}$, respectively. We obtain $\lambda_R \sim 100 \mu\text{eV}$ and $\lambda_{VZ} \sim 350 \mu\text{eV}$. The obtained values are of similar order magnitude as reported in literature [7–9].

* corresponding author; s.omar@rug.nl

- [1] M. Gurram, S. Omar, S. Zihlmann, P. Makk, C. Schönenberger, and B. J. van Wees, *Phys. Rev. B* **93**, 115441 (2016).
- [2] P. J. Zomer, M. H. D. Guimarães, J. C. Brant, N. Tombros, and B. J. van Wees, *Appl. Phys. Lett.* **105**, 013101 (2014).
- [3] T. Maassen, I. J. Vera-Marun, M. H. D. Guimarães, and B. J. van Wees, *Phys. Rev. B* **86**, 235408 (2012).
- [4] S. Omar and B. J. van Wees, *Phys. Rev. B* **95**, 081404 (2017).
- [5] C. Kittel, *Introduction to Solid State Physics* (Wiley, 2004).
- [6] B. Raes, J. E. Scheerder, M. V. Costache, F. Bonell, J. F. Sierra, J. Cuppens, J. Van de Vondel, and S. O. Valenzuela, *Nat. Commun.* **7**, 11444 (2016).
- [7] A. W. Cummings, J. H. Garcia, J. Fabian, and S. Roche, *Phys. Rev. Lett.* **119**, 206601 (2017).
- [8] S. Omar and B. J. van Wees, *Phys. Rev. B* **97**, 045414 (2018).
- [9] S. Zihlmann, A. W. Cummings, J. H. Garcia, M. Kedves, K. Watanabe, T. Taniguchi, C. Schönenberger, and P. Makk, *Phys. Rev. B* **97**, 075434 (2018).